On Demand Shape-Selective Integration of Individual Vertical Germanium Nanowires on a Si(111) Substrate *via* Laser-Localized Heating

Sang-gil Ryu,[†] Eunpa Kim,[†] Jae-hyuck Yoo,[†] David J. Hwang,[§] Bin Xiang,[†,‡] Oscar D. Dubon,[‡] Andrew M. Minor,[‡] and Costas P. Grigoropoulos[†,*]

[†]Department of Mechanical Engineering and [‡]Department of Materials Science and Engineering, University of California, Berkeley, California 94720, United States, and [§]Department of Mechanical Engineering, State University of New York at Stony Brook, New York 11794, United States

ABSTRACT Semiconductor nanowire (NW) synthesis methods by blanket furnace heating produce structures of uniform size and shape. This study overcomes this constraint by applying laser-localized synthesis on catalytic nanodots defined by electron beam lithography in order to accomplish site- and shape-selective direct integration of vertically oriented germanium nanowires (GeNWs) on a single Si(111) substrate. Since the laser-induced local temperature field drives the growth process, each NW could be synthesized with distinctly different geometric features. The NW shape was dialed on demand, ranging from cylindrical to hexagonal/irregular hexagonal pyramid. Finite difference time domain analysis supported the tunability of the light absorption and scattering spectra *via* controlling the GeNW shape.

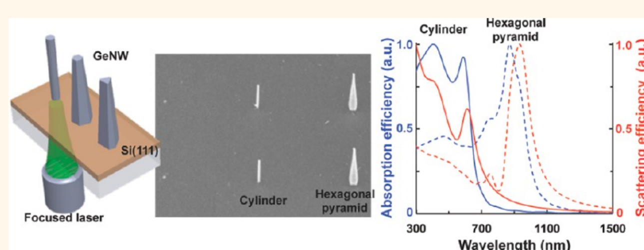

KEYWORDS: germanium nanowires · vertical orientation · site- and shape-selective integration · laser-assisted growth · facet · taper

The size, shape, surface roughness, and facets of nanowires (NWs) regulate the electrical[1,2] and thermal[3−5] transport, as well as the optical properties.[6,7] In particular, light interactions with semiconductor materials can be engineered for absorption and scattering enhancement and reflectance reduction, depending on the NW shape.[8,9] Hence, NWs have been used in the context of photovoltaic,[7,10] optoelectronic,[11−13] and sensing applications.[14−16]

Despite interesting characteristics of NWs, it has not been straightforward to embed multiple properties and functionalities in a single NW-based device. The composition can be varied along the axial direction by controlling the lateral growth rate by a gas on−off process.[17] However, the broad interfacial length induced by the vapor−liquid−solid (VLS) growth mechanism hinders sharp property differentiation. On-demand discrete assembly and integration of individual NWs with different properties in a planar layout would require elaborate optical/optoelectronic tweezing.[18,19] On the other hand, out-of-plane and vertically oriented architectures are more desirable for the direct synthesis and discrete integration of functionalized NWs with enhanced device performance.[20−23] Vertical silicon nanowire (SiNW) arrays or single Si nanopillars having different diameters that were fabricated by top-down etching combined with electron beam lithography (EBL) could induce changes of reflected color or enhance the Raman scattering.[24,25] Bottom-up processes, including VLS assisted by EBL, could also yield NWs of different size,[26] although lack control of the NW geometric features, including tapering and facets.

In chemical vapor deposition (CVD) processes, a focused laser beam has been utilized to achieve site-selective growth of semiconductor materials since the respective kinetics follow an Arrhenius behavior.[27,28] Specifically, spatially confined and temporally modulated continuous wave (CW) laser irradiation can impose a short heating and cooling time scale and hence sufficient precision for controlling the localized growth time and temperature.[29] By taking advantage

* Address correspondence to cgrigoro@me.berkeley.edu.

Received for review September 22, 2012 and accepted February 16, 2013.

Published online February 17, 2013
10.1021/nn400186c

© 2013 American Chemical Society

of the laser-induced local heating, on-demand growth of Si and/or Ge NWs based on the VLS mechanism has been demonstrated in our previous studies.[30,31] Moreover, since the growth temperature is a decisive factor in determining the facet and taper evolution and therefore the NW geometric shape,[32,33] focused laser irradiation can achieve direct integration of individually tailored NWs.

In this paper, we demonstrate discrete VLS growth of vertical germanium nanowires (GeNWs) with deliberately varying shapes on a single Si(111) substrate by adopting laser-localized heating. It is noted that a single-step temperature process was applied in this study with the intent to vary the GeNW taper angle instead of the two-step process required for nontapered GeNW growth.[32−34] Finite difference time domain (FDTD) analysis confirms the tunability of the light scattering and absorption spectra.

RESULTS AND DISCUSSION

A 4 μm thick p-doped Si(111) film was prepared on a 500 μm thick quartz wafer by thermal bonding. The film thickness was chosen in order to ensure sufficient absorption of the laser energy in the film. Gold (Au) dots of 65 nm diameter were prepared on the Si(111) film by e-beam lithography. After the chamber was purged by flowing argon and evacuated (<1 mTorr) by a dry pump, 3% germane (GeH_4) in hydrogen was introduced at 300 sccm, maintaining the total chamber pressure at 400 Torr for growth. Once a steady gas environment was established in the vacuum chamber, a Nd:YAG laser beam of 532 nm wavelength was delivered through an optical window and focused at the interface of the Si(111) film and the quartz substrate. The laser power was adjusted by an attenuator, and the growth time was controlled by an optical switch in the range of 1−30 s. In order to confine the reaction and prevent growth on catalysts spaced 2 μm away from the desired location, the Gaussian laser beam was tightly focused *via* a high-NA objective lens to a ∼1 μm focal spot diameter (defined at the $1/e^2$ position of the intensity profile and measured by the knife edge method) at the Si/quartz interface. Numerical simulations of the conductive heat transfer were carried out to determine the laser-induced temperature distribution. Details, including the computed relationship between laser power and induced peak temperature at the center of the reaction zone, are given in the Supporting Information.

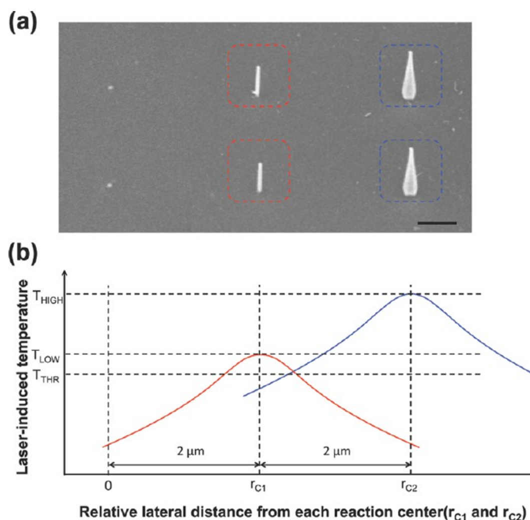

Figure 1. Laser-induced digital growth of vertical GeNWs on a single Si(111) substrate with different shapes (a) and the individual growth scheme to avoid thermal influence on the neighboring catalysts (b). Gaussian laser beam ($M^2 \approx 1$) was tightly focused *via* a high-NA objective lens to a ∼1 μm focal spot diameter (defined at the position where the intensity drops by a factor of $1/e^2$ with respect to the center and measured by the knife edge method) at the Si/quartz interface. The growth was performed with precise temperature control *via* laser beam irradiation for 10 s. Shown in (a) are as-deposited gold particles by e-beam lithography having 2 μm spacing [left], cylindrical GeNWs grown at lower growth temperature (T_{LOW}) [center], and hexagonal pyramid GeNWs grown at higher growth temperature (T_{HIGH}) [right]. The individually controlled growth was repeated for each laser power (and temperature setting). T_{THR} indicates the reaction threshold temperature. A field-emission scanning electron microscopy (FE-SEM) image was taken at a 45° tilt angle. Scale bar is 500 nm.

Figure 1a displays a representative field emission scanning electron microscopy (FE-SEM) image demonstrating the discrete fabrication of vertical GeNWs with different features on a Si(111) substrate. Au dots of 65 nm diameter with 2 μm spacing were prepared by e-beam lithography as shown in the left column of Figure 1a. Each catalyst was then heated by localized focused laser illumination and varying growth conditions. As a result, GeNWs attained a cylindrical shape at lower growth temperature, T_{LOW} [at the center of Figure 1], and turned into hexagonal pyramids at higher temperature, T_{HIGH} [at the right in Figure 1]. The individually controlled growth was repeated for each temperature setting, as shown in Figure 1a. The capability of dialing on-demand the shape and size of individual nanowires is contrasted with conventional VLS growth or etching processes. For precise control of the growth temperature, each catalyst was placed in the center of the laser beam *via* a microscopic vision alignment scheme utilizing alignment keys marked on the periphery of the catalyst array pattern (not shown in Figure 1). The positioning was controlled by a nanometer-level positioning system with 1 nm resolution, 250 nm position accuracy, and 75 nm repeatability. Growth at the center of the laser-induced Gaussian-like temperature profile and above the reaction threshold temperature (T_{THR}) is indeed advantageous for defining discrete nanowires, as shown in Figure 1.

Our thermal analysis based on the experimental configuration shows that the Gaussian-like steady temperature profile exhibits a drop ($T_C - T$) of ∼80 °C at the radial distance of 2 μm from the reaction center (*i.e.*, the center of the focused laser beam) when the

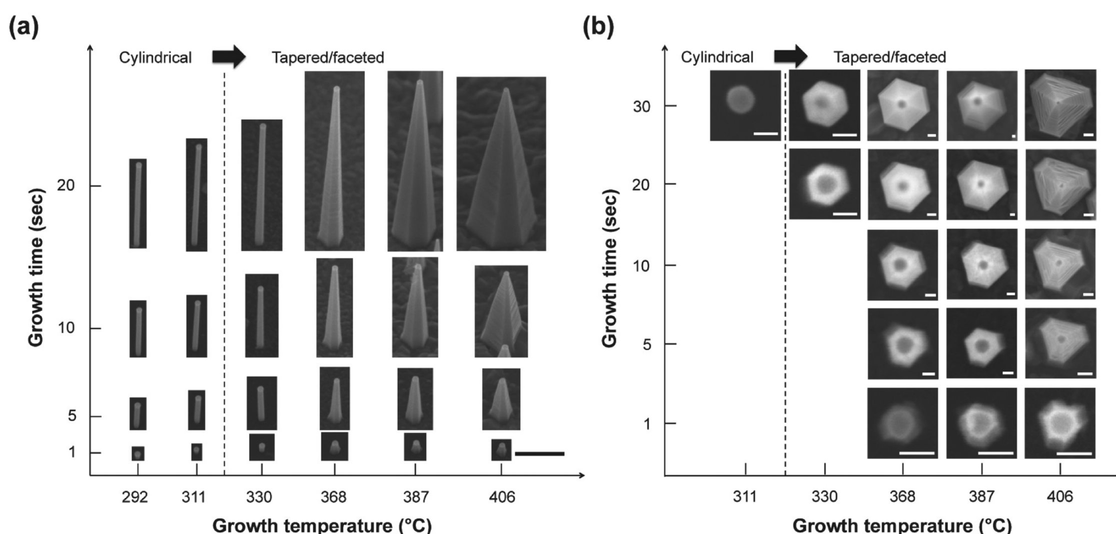

Figure 2. (a) Field-emission scanning electron microscopy (FE-SEM) images at a 45° tilt angle of vertically grown GeNWs on a Si(111). All NWs were grown on a single 4 μm thick c-Si bonded on quartz. The growth temperature ranges from 292 to 406 °C, and the growth time from 1 to 20 s. Scale bar is 500 nm. (b) Planar view images of vertically grown GeNWs on Si(111). The growth temperature ranges from 311 to 406 °C, and the growth time from 1 to 30 s. Scale bars are 50 nm.

reaction center temperature (T_C) reaches ~350 °C (see Supporting Information Figure S1). The center temperature of ~350 °C is sufficient for producing GeNWs of hexagonal pyramid shape. On the other hand, the predicted temperature at a radial distance of 2 μm away from the laser beam center is below the reaction threshold temperature for growth ($T_{THR} \approx 270$ °C), hence indicating the absence of reaction. It is noted that higher peak temperature at the reaction zone center implies that the area experiencing a temperature above the reaction threshold temperature is larger. Therefore, wider spacing between the catalysts or a more tightly focused laser beam (*e.g.*, Bessel beam shape) would be required to avoid growth on the neighboring catalytic sites.

In order to investigate the growth kinetics, it is necessary to determine the laser-induced temperature. The laser-localized reaction is driven by the three-dimensional transport of the precursor gas and exchange of reaction byproducts over a micrometer-scale reaction zone *versus* the essentially one-dimensional transport over a wider reaction zone in furnace processes.[28,29] Our previous study has also shown a faster growth rate of SiNWs by laser-localized heating than by furnace blanket heating under similar growth conditions.[30] Due to the different gas transport over the reaction spot, which yields different nanowire growth rates and morphology, it is not meaningful to infer the temperature by comparing the present laser-enabled method with furnace results. Instead, we adopted an experimental procedure[35] whose validity was confirmed in a number of laser-assisted Si CVD experiments. The temperature as a function of laser power is experimentally determined *via* a linear relationship between the laser-induced temperature increase and applied laser power, taking the silicon melting temperature as the experimental reference point and assuming the room temperature at 27 °C (see details in Methods section). We also confirmed that the experimentally determined temperature is in good agreement with the numerical thermal analysis prediction (see Supporting Information Figure S1d).

Temperature-Dependent Geometrical Features of Individual GeNWs. The geometric features of vertical GeNWs were controlled across a wide range by varying the laser-induced local growth temperature and time. The spacing between the catalysts was not limited to 2 μm in order to avoid thermal influence on the neighboring catalysts at elevated growth temperatures.

FE-SEM images taken at angles of 45° and 0° in Figure 2 exhibit morphologies of vertical GeNWs grown on Si(111) with respect to the growth temperature and time. The onset of GeNW growth is traced as early as 1 s over the temperature range that can activate growth (292−406 °C), and the axial growth rate is observed as fast as ~210 nm/s. The GeNW shape changes with growth temperature, exhibiting a striking transition from having a uniformly cylindrical cross section to tapered and faceted morphology after 311 °C. The sidewall facets of vertical GeNWs grown on Si(111) are transformed from circular to hexagonal and irregular hexagonal shapes with increasing growth temperature, as shown in Figure 2b. The tapered NW geometry is typically due to vapor−solid (VS) sidewall deposition during the growth.[36] For that reason, the nanowire aspect ratio initially increases with growth temperature with negligible sidewall deposition until 311 °C, but decreases beyond this temperature since the radial growth rate is enhanced as shown in Figure 3a. The axial growth rate decreases after 387 °C, while the radial growth rate still increases with temperature. Figure 3b shows that the axial growth rate at 406 °C for times exceeding a few seconds is

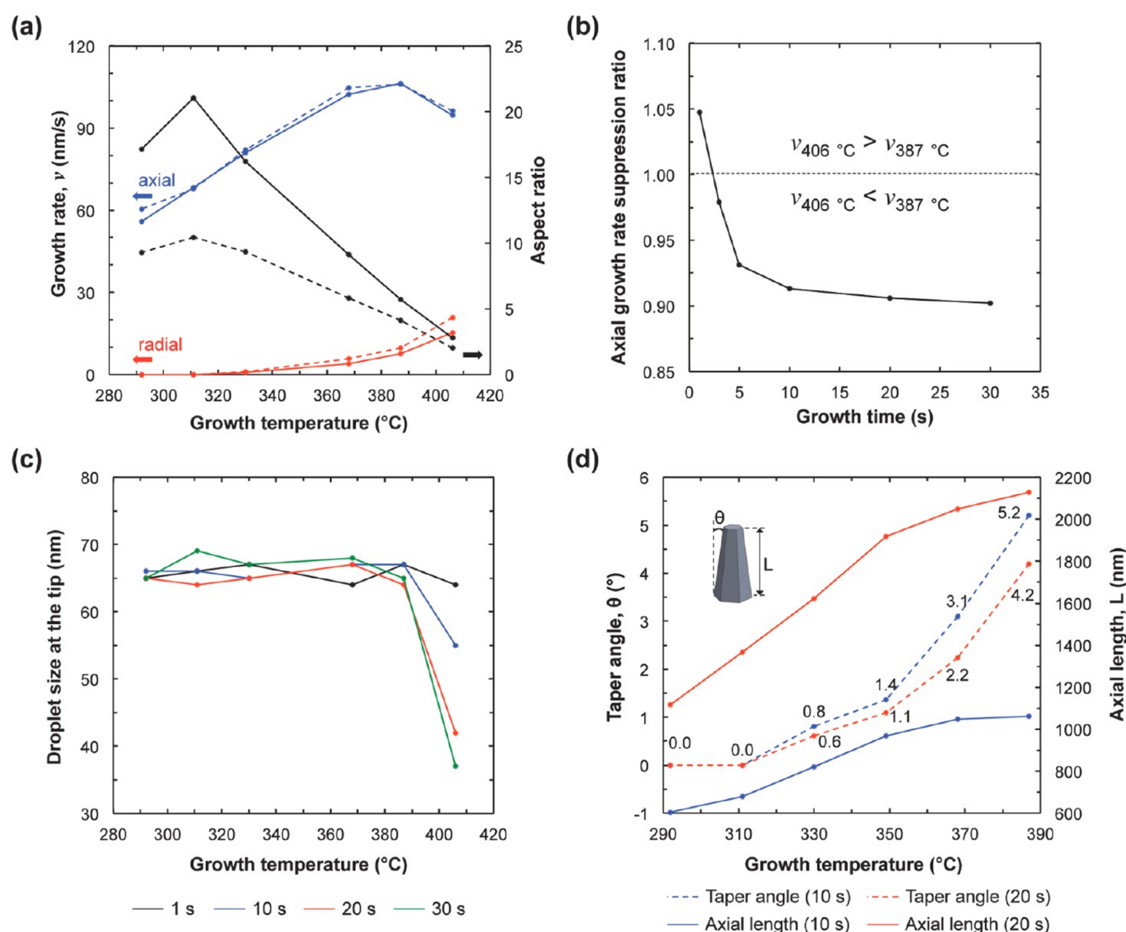

Figure 3. (a) Axial, radial growth rate and aspect ratio with respect to growth temperature at growth times of 10 and 20 s. The aspect ratio (black line) increases until 311 °C since the axial growth rate (blue line) increases and the radial growth remains negligible. However, it decreases after 311 °C with increasing radial growth rate (red line). The dashed and solid lines indicate the growth time of 10 and 20 s, respectively. (b) Growth rate suppression ratio defined by the ratio of axial growth rate at 406 °C to that at 387 °C with respect to growth time. This rate drops below 1 for times exceeding a few seconds. (c) Ge/Au alloyed droplet size at the tip of the GeNWs with respect to growth temperature and time. The data were measured and averaged from 10 GeNWs. (d) Taper angles and axial lengths with respect to growth temperature (292−387 °C) at different growth times of 10 and 20 s.

suppressed compared to the axial growth rate at 387 °C. The axial growth rate suppression ratio (defined by the ratio of axial growth rate at 406 °C to that at 387 °C) is ∼1.05 at a growth time of 1 s, implying that the growth rate still increases with growth temperature even after 387 °C, but reduces to ∼0.9 at 30 s. The change of catalyst size with respect to growth temperature and time should be considered in order to explain this trend. As shown in Figure 3c, the catalyst droplet diameter stays constant at approximately the initial size of ∼65 nm between 292 and 387 °C, regardless of the growth time. The axial growth rate in this range follows an Arrhenius-like temperature dependence with calculated activation energy at ∼20 kJ/mol by the least-squares fit method with an R^2 value of ∼0.96 (see Supporting Information). However, the droplet size shrinks to ∼37 nm at 406 °C with increasing growth time. The Au catalyst is possibly consumed by the surface diffusion of Au nanoclusters along the NW sidewall.[37] Although such Au nanoclusters were not detected on the sidewall within the limitations of the scanning electron microscopy, the appearance of regular or irregular hexagonal facets could imply Au surface diffusion since the faceting is known to be associated with the presence of Au on the sidewall.[37−41] As shown in Figure 3a and c, the axial growth rate eventually decreases as the droplet size shrinks at elevated temperatures. This reduction is a result of size-dependent supersaturation, quantified by the Gibbs−Thomson effect according to

$$\Delta\mu = \Delta\mu_0 - \frac{4\alpha\Omega}{d}$$

where $\Delta\mu_0$ is the supersaturation chemical potential in the planar limit, α is the surface free energy of Au, Ω is the atomic volume of Ge, and d is the catalyst diameter. The supersaturation, which is the driving mechanism for incorporating Ge atoms into the Au catalyst, decreases with diminishing catalyst size and slowing growth rate. The taper angle, determined by the longest diagonals of the NW base and tip cross sections and the axial length, varies with the different growth conditions, as shown in Figure 3d. While the longest diagonal at the tip is fixed at

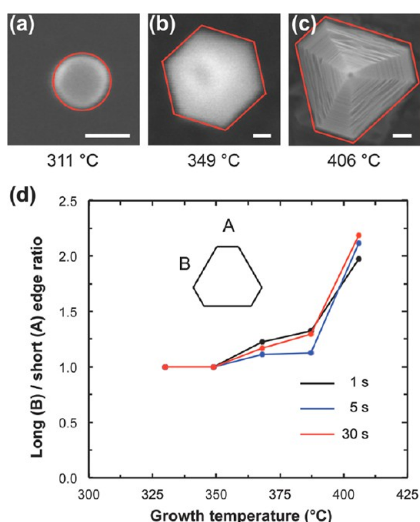

Figure 4. Facet evolution with respect to growth temperature and time. (a–c) Zoom-in cross sectional images of GeNWs grown for 30 s at 311, 349, and 406 °C, respectively. Red solid lines indicate the contour of facets perpendicular to the growth direction ⟨111⟩. The sidewall facets transition from circular (a) to hexagonal (b) and irregular hexagonal shape (c) with increasing growth temperature. (d) Ratio of the length of a long edge to that of a short edge with respect to growth temperature and time. Scale bars are 50 nm.

65 nm between 292 and 387 °C, the diagonal at the root and the axial length both increase with growth temperature. Consequently, the taper angle increases up to 5.2° and 4.2° for growth times of 10 and 20 s with increasing temperature, respectively.

The variation of the temperature-dependent facet evolution was investigated in detail by the cross sectional images ((111)-plane) in Figure 4. Cylindrical GeNWs of circular cross sections are grown (Figure 4a) until 311 °C, exhibiting negligible radial expansion, as shown in Figure 2a. The exact shape for small wire diameters is somewhat ambiguous within the resolution of scanning electron microscopy, as it could conceivably be dodecagonal, *e.g.*, as for SiNWs.[42,43] With increasing temperature, however, facets perpendicular to the ⟨111⟩ growth direction emerge due to VS sidewall deposition, causing tapering along the axial direction. In the intermediate temperature range (330–349 °C), a faceted hexagonal shape (Figure 4b) is observed for times exceeding 1 s. Accordingly, GeNWs are shaped as tapered hexagonal pyramids. In the higher temperature range (368–406 °C), the facets construct pyramids of hexagonal cross sections with alternating long and short edges (Figure 4c). The irregular hexagonal shape is a consequence of surface orientation dependent growth rate that is attributed to anisotropic solid–vapor surface energy. The epitaxial growth rate of Si depends on the crystalline orientation.[44] Consequently, slower growing facets expand, while those growing faster shrink. The facet orientation in GeNWs can be understood since Ge has the same crystal structure as Si, although a different lattice constant. Therefore, it is assumed that the $(11\bar{2})$, $(\bar{2}11)$, and $(1\bar{2}1)$ facets grow slower and construct long edges, while $(2\bar{1}\bar{1})$, $(\bar{1}\bar{1}2)$, and $(\bar{1}2\bar{1})$ facets grow faster and form short edges.[39,42,45] Since the surface energy anisotropy strongly depends on the growth temperature, the ratio of the length of a long edge (A) to that of a short edge (B) increases with temperature, as shown in Figure 4d. The facet configuration is determined at the early stage of the NW growth and maintained thereafter, although the NW thickens due to continuous VS sidewall deposition. Anisotropic growth is possibly enhanced by the different wetting configuration or coverage of the Au catalyst material with respect to the facet orientation.[46,47] Our study did not provide clear evidence of this effect, since Au nanoclusters were not detected on the sidewalls as previously noted. The surfaces of the faceted sidewalls tend to roughen, forming terraces to adapt to the shrinking NW cross section. The terraces are more evident after the abrupt change in the catalyst behavior observed upon the growth of GeNWs at 406 °C, since this alters significantly the NW diameter, as documented in Figure 4c. The terrace formation is affected by the facet orientation, exhibiting enhanced roughness on the surfaces of the higher energy long-edged facets compared to the short-edged ones (see Supporting Information). Surface energy minimization can lead to exposure of relief structures[48] and is manifested either by changing the overall facet shape or developing secondary sawtooth facets.[39,42,43]

Cross Sectional HRTEM of GeNW/Si Film. The GeNW crystallographic growth direction and epitaxy were confirmed by cross sectional transmission electron microscopy (TEM). Figure 5a shows the low-magnification TEM image of a GeNW vertically sliced and thinned by a focused ion beam (FIB) after it was coated with platinum (Pt) in the FIB with the red dashed line marking the NW contour. The diffraction patterns of the GeNW (left inset of Figure 5b) and the Si substrate (right inset of Figure 5b) taken along a ⟨011⟩ zone axis verify that the GeNW is epitaxially grown along the ⟨111⟩ direction on the underlying Si(111) substrate. The NW widens from ~70 nm at the base to ~400 nm at a height of ~320 nm and thereafter narrows to yield a tapered pyramid shape. This reversed tapering near the Si surface is caused by strain relaxation associated with the lattice mismatch between Ge and Si.[49,50] Figure 5b confirms that the GeNW is dislocation-free despite lattice mismatch. Previous studies have indicated that a critical diameter is required for dislocation-free epitaxial growth of NWs on lattice-mismatched substrates, although the nanosized catalytic epitaxial growth can favorably accommodate the misfit strain through strain relaxation, preventing islanding or dislocations unlike in thin film epitaxial growth.[51,52] Since the diameter of the root is below the critical value (~100 nm) for a 4.2% lattice mismatch, it is believed that the GeNW could be epitaxially grown without dislocations on Si film, in good agreement with the previous experimental and theoretical studies. Despite having experienced the

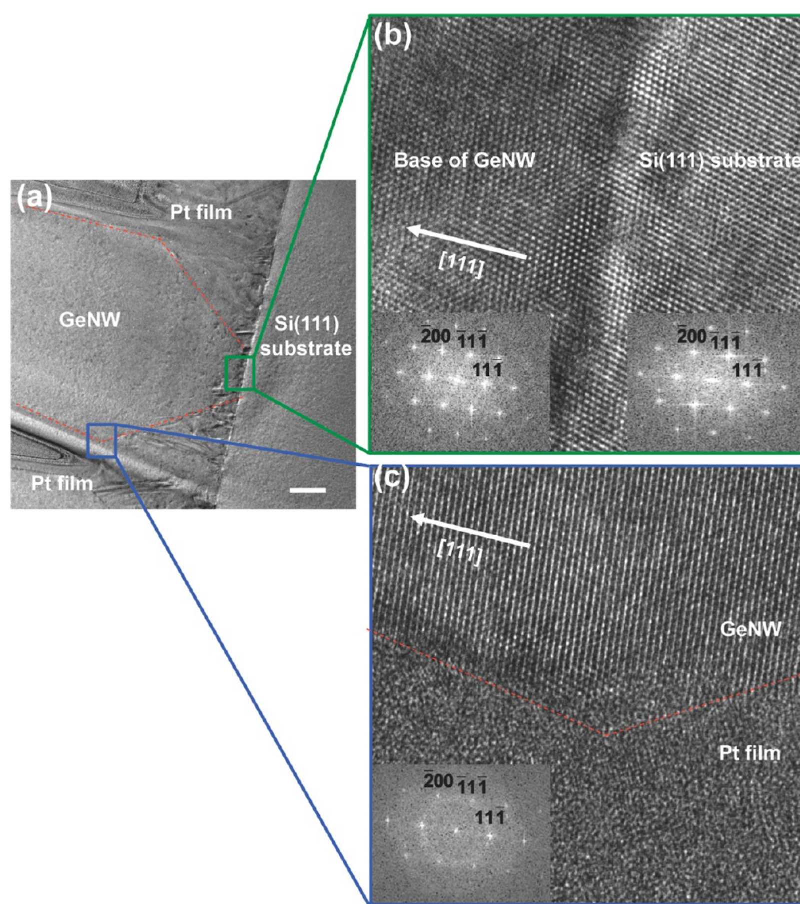

Figure 5. Vertical cross sectional transmission electron microscopy (TEM) images of a GeNW heteroepitaxially grown on Si(111) in the vicinity of the interface. (a) Low-magnification TEM image of the cross section. The red dashed line traces the contour of the GeNW at the base. (b) High-resolution TEM image of the interface between the GeNW and the Si substrate. Left and right insets are the diffraction patterns of the GeNW and the Si substrate, respectively. (c) High-resolution TEM image of the vicinal area encompassing the NW tapering reversal that occurs at a distance of ∼320 nm from the base. The inset is the diffraction pattern of the GeNW in this area. Scale bar is 100 nm.

above-described abrupt geometry change at a distance of only ∼320 nm from the base, the GeNW appears defect-free, as displayed in Figure 5a. Dislocation-free epitaxial growth is crucial for optoelectronic and electronic applications. Accordingly, our results confirm that the present laser-assisted direct integration approach is suitable for monolithic integration of semiconductor NWs on lattice-mismatched substrates.

Geometrical Feature Dependent Optical Spectra of Vertical NWs. The on-demand shaped and discrete NWs fabricated in this study may enable embedding multiple optical properties on a single substrate since nanostructures such as nanoparticles or nanowires are known to tailor optical properties depending on the shape or size.[6,53−55] Therefore, we performed spectral FDTD analysis to investigate the effect of the geometrical features on the optical response. The Q_{abs} and Q_{sca} spectra were calculated for linearly polarized, normal illumination incident parallel to the NW axis. The examined structures were based on the geometric features of NWs grown at 311−368 °C for 20 s. Our experimental results (Figure 3d) show that in this growth temperature range the NW geometries transitioned from 65 nm diameter cylindrical to hexagonal pyramid with taper angles of 0.6°, 1.1°, and 2.2°. The numerical analysis in Figure 6 shows that the optical spectra peaks shift from visible to near-infrared wavelengths upon the geometrical feature transformation. The observed shifts are in the range from 592 to 1068 nm and 621 to 1133 nm in the Q_{abs} and Q_{sca} spectra, respectively. The NW shape incorporates combined and coupled changes in the axial/radial length, facet evolution, and taper angle. We therefore identified the influence of these effects on the optical response (see Supporting Information). Dimensional effects including the axial length and diameter change of the NWs were analyzed considering a simple cylindrical structure. While the spectral peaks are mostly preserved within the narrow axial length variation of ∼0.8 μm at fixed diameter (Figure S4), increasing the diameter at fixed axial length results in red shifts from 592 to 1291 nm and 621 to 1338 nm in the Q_{abs} and Q_{sca}, respectively (Figure S5). The dimensional effect on the optical response is in good agreement with that

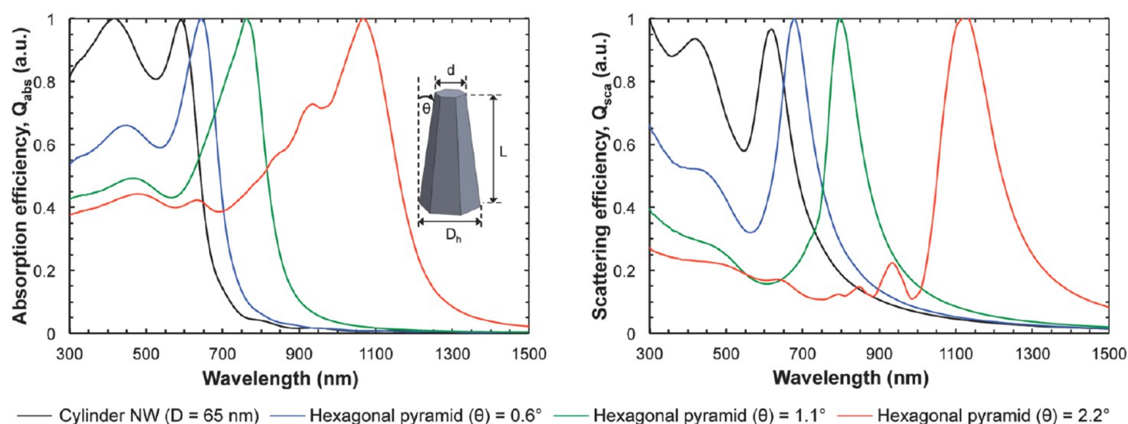

Figure 6. Finite-difference time domain (FDTD) analysis of the absorption, Q_{abs}, and scattering efficiency, Q_{sca}, spectra from a single GeNW with different geometric shapes under linearly polarized normal incident illumination on the top of the GeNW. A cylindrical GeNW with diameter of 65 nm (black solid) and hexagonal pyramid GeNWs with different taper angles (θ) of 0.6° (blue), 1.1° (green), and 2.2° (red). In the hexagonal pyramid GeNWs, the longest diagonal (d) at the top surface stays constant at 65 nm, while the longest diagonal (D_h) at the bottom surface as well as axial length (L) increase from 65 nm to 225 nm and from 1369 nm to 2050 nm with growth temperature, respectively. The Q_{abs} and Q_{sca} spectra were normalized to unity to highlight the spectral shape and the shift of the peak.

obtained by vertical SiNW arrays, but the peak positions are slightly different due to the different complex refractive index of the materials.[24,53] The facet evolution and taper angle cause blue shifts of ~4% and ~15% (in the case of 2.2°), respectively (Figure S6). As a result, the peaks from a 2.2° tapered hexagonal structure are finally tuned from 1291 nm to 1068 nm and from 1338 nm to 1133 nm in the Q_{abs} and Q_{sca} spectra, respectively.

Accordingly, an increase/decrease in the NW circumference in conjunction with the taper angle variation enables effective tuning of the absorption and scattering spectra. Since the geometrical shape is fully controlled by applying laser-localized heating on catalysts of uniform size, a cost-effective technique, for example, utilizing a glass or polymer sphere self-assembly method, can be eventually implemented to assemble ordered catalyst nanoparticle arrays.

CONCLUSIONS

In conclusion, single vertical GeNWs were integrated on Si(111) with on-demand shape selectivity by employing laser-induced local heating. GeNWs with shapes ranging from cylindrical to hexagonal/irregular hexagonal pyramids were fabricated from catalysts of uniform size by controlling the NW taper angle, facet structure, and length. The Gaussian profile of the focused laser beam could constrain the lateral size of the reaction zone to dimensions smaller than the actual beam size by taking advantage of the reaction temperature threshold. However, the distance between NWs in this study was limited to the O(1 μm) diffusion length effected by the CW laser beam irradiation. The lateral thermal diffusion length ($\propto\sqrt{t}$, t is the pulse width) could be shortened by employing pulsed or temporally modulated laser irradiation. As shown in our own experiments (not reported here), near-field laser illumination can further reduce the lateral size of the reaction zone beyond the diffraction limit, resulting in nanoscale layouts of NWs. A flattop beam profile can also be employed to irradiate an ensemble of NWs for efficient production of identical shapes.

In this study, tapered GeNWs were fabricated by inducing VLS axial and VS radial growth in the intermediate temperature range. Precise control of the taper angle was achieved by adjusting the growth temperature to access different growth rates. The shape of the GeNWs was also determined by the temperature-dependent facet evolution at the onset of the growth. The faceted NW cross sectional shapes transitioned from hexagonal to trigonal-hexagonal, due to the VS surface energy anisotropy at higher growth temperatures. Dislocation-free epitaxial growth of GeNW on Si was confirmed, a crucial attribute for integration into optoelectronic and electronic applications.

The tunability of the absorption and scattering spectra was illustrated by the FDTD analysis, showing spectral peak shift over a broad range by controlling the taper angle, facet, diameter, and length. It is therefore demonstrated that single GeNWs possessing individually tailored optical properties can be directly integrated on a single substrate. Therefore, the laser-localized selective growth scheme presented in this work opens a route toward the facile fabrication of multifunctional NW-based devices.

METHODS

Sample Preparation. A silicon on insulator (SOI) wafer and a quartz wafer were cleaned by RCA followed by oxygen plasma. After the metallized side of the quartz wafer was brought into contact with the device layer side of the SOI wafer by surface tension, it was annealed at 120 °C in a convection oven for 24 h.

ARTICLE

Only the device layer (p-doped Si(111), 1−10 ohm-cm) of the SOI wafer remained on a 500 μm quartz wafer after etching the handle wafer and buried oxide layer using KOH followed by HF. In order to obtain vertical and heteroepitaxial growth of GeNWs, the native oxide layer on the silicon surface was removed by using 10:1 buffered oxide etch before depositing the 65 nm Au catalysts on the sample surface.

Laser-Induced Temperature Determination. To determine laser-induced temperature in a thin Si film on a quartz substrate, we adopted the experimental procedure used in laser-assisted Si CVD experiments.[35] The melting threshold laser power of the Si film was experimentally measured, applying the melting point of 1410 °C as the corresponding temperature. The temperature at lower laser power levels was estimated by assuming linear dependence of the temperature on the laser power. For our study, utilizing the experimentally measured melting threshold laser power (P_m) for a Si film devoid of Au catalysts and immersed in a similar gas environment (H_2, ~400 Torr, and ~300 sccm), the temperature as a function of laser power (P) was determined by applying a linear relationship between the laser-induced temperature increase and applied laser power, taking the melting temperature as the experimental reference point and assuming room temperature as 27 °C:

$$T(°C) = (1410 - 27)\frac{P}{P_m} + 27$$

Conflict of Interest: The authors declare no competing financial interest.

Acknowledgment. The authors gratefully acknowledge support by DARPA/MTO under grant N66001-08-1-2041. The experiment was carried out at the UC Berkeley Marvell Nanolab. SEM and TEM analysis performed at the National Center for Electron Microscopy, Lawrence Berkeley National Laboratory, was supported by the Scientific User Facilities Division of the Office of Basic Energy Sciences, U.S. Department of Energy, under Contract No. DE-AC02-05CH11231.

Supporting Information Available: Numerical analysis of laser-induced temperature, calculation of activation energy for the axial growth, surface roughness profiles along facet surfaces, and FDTD analysis of the individual effect of facet evolution, length, and taper angle on the absorption and scattering efficiency spectra. These materials are available free of charge *via* the Internet at http://pubs.acs.org.

REFERENCES AND NOTES

1. Zhao, X.; Wei, C. M.; Yang, L.; Chou, M. Y. Quantum Confinement and Electronic Properties of Silicon Nanowires. *Phys. Rev. Lett.* **2004**, *92*, 236805.
2. Haick, H.; Hurley, P. T.; Hochbaum, A. I.; Yang, P.; Lewis, N. S. Electrical Characteristics and Chemical Stability of Non-Oxidized, Methyl-Terminated Silicon Nanowires. *J. Am. Chem. Soc.* **2006**, *128*, 8990–8991.
3. Hochbaum, A. I.; Chen, R.; Delgado, R. D.; Liang, W.; Garnett, E. C.; Najarian, M.; Majumdar, A.; Yang, P. Enhanced Thermoelectric Performance of Rough Silicon Nanowires. *Nature* **2008**, *451*, 163–167.
4. Martin, P.; Aksamija, Z.; Pop, E.; Ravaioli, U. Impact of Phonon-Surface Roughness Scattering on Thermal Conductivity of Thin Si Nanowires. *Phys. Rev. Lett.* **2009**, *102*, 125503.
5. Sansoz, F. Surface Faceting Dependence of Thermal Transport in Silicon Nanowires. *Nano Lett.* **2011**, *11*, 5378–5382.
6. Cao, L.; Fan, P.; Barnard, E. S.; Brown, A. M.; Brongersma, M. L. Tuning the Color of Silicon Nanostructures. *Nano Lett.* **2010**, *10*, 2649–2654.
7. Muskens, O. L.; Rivas, J. G.; Algra, R. E.; Bakkers, E. P. A. M.; Lagendijk, A. Design of Light Scattering in Nanowire Materials for Photovoltaic Applications. *Nano Lett.* **2008**, *8*, 2638–2642.
8. Garnett, E.; Yang, P. Light Trapping in Silicon Nanowire Solar Cells. *Nano Lett.* **2010**, *10*, 1082–1087.
9. Jung, J.-Y.; Guo, Z.; Jee, S.-W.; Um, H.-D.; Park, K.-T.; Lee, J.-H. A Strong Antireflective Solar Cell Prepared by Tapering Silicon Nanowires. *Opt. Express* **2010**, *18*, A286–A292.
10. Garnett, E. C.; Yang, P. Silicon Nanowire Radial P-N Junction Solar Cells. *J. Am. Chem. Soc.* **2008**, *130*, 9224–9225.
11. Li, Y.; Qian, F.; Xiang, J.; Lieber, C. M. Nanowire Electronic and Optoelectronic Devices. *Mater. Today* **2006**, *9*, 18–27.
12. Cui, Y.; Lieber, C. M. Functional Nanoscale Electronic Devices Assembled Using Silicon Nanowire Building Blocks. *Science* **2001**, *291*, 851–853.
13. Cui, Y.; Zhong, Z. H.; Wang, D. L.; Wang, W. U.; Lieber, C. M. High Performance Silicon Nanowire Field Effect Transistors. *Nano Lett.* **2003**, *3*, 149–152.
14. Cao, L.; Park, J.-S.; Fan, P.; Clemens, B.; Brongersma, M. L. Resonant Germanium Nanoantenna Photodetectors. *Nano Lett.* **2010**, *10*, 1229–1233.
15. Zheng, G. F.; Patolsky, F.; Cui, Y.; Wang, W. U.; Lieber, C. M. Multiplexed Electrical Detection of Cancer Markers with Nanowire Sensor Arrays. *Nat. Biotechnol.* **2005**, *23*, 1294–1301.
16. Alivisatos, P. The Use of Nanocrystals in Biological Detection. *Nat. Biotechnol.* **2004**, *22*, 47–52.
17. Kim, B.-S.; Kim, M. J.; Lee, J. C.; Hwang, S. W.; Choi, B. L.; Lee, E. K.; Whang, D. Control of Lateral Dimension in Metal-Catalyzed Germanium Nanowire Growth: Usage of Carbon Sheath. *Nano Lett.* **2012**, *12*, 4007–4012.
18. Pauzauskie, P. J.; Radenovic, A.; Trepagnier, E.; Shroff, H.; Yang, P. D.; Liphardt, J. Optical Trapping and Integration of Semiconductor Nanowire Assemblies in Water. *Nat. Mater.* **2006**, *5*, 97–101.
19. Jamshidi, A.; Pauzauskie, P. J.; Schuck, P. J.; Ohta, A. T.; Chiou, P.-Y.; Chou, J.; Yang, P.; Wu, M. C. Dynamic Manipulation and Separation of Individual Semiconducting and Metallic Nanowires. *Nat. Photonics* **2008**, *2*, 85–89.
20. Goldberger, J.; Hochbaum, A. I.; Fan, R.; Yang, P. D. Silicon Vertically Integrated Nanowire Field Effect Transistors. *Nano Lett.* **2006**, *6*, 973–977.
21. Rosaz, G.; Salem, B.; Pauc, N.; Potie, A.; Gentile, P.; Baron, T. Vertically Integrated Silicon-Germanium Nanowire Field-Effect Transistor. *Appl. Phys. Lett.* **2011**, *99*, 193107.
22. Ng, H. T.; Han, J.; Yamada, T.; Nguyen, P.; Chen, Y. P.; Meyyappan, M. Single Crystal Nanowire Vertical Surround-Gate Field-Effect Transistor. *Nano Lett.* **2004**, *4*, 1247–1252.
23. Kamins, T. I.; Li, X.; Williams, R. S. Growth and Structure of Chemically Vapor Deposited Ge Nanowires on Si Substrates. *Nano Lett.* **2004**, *4*, 503–506.
24. Khorasaninejad, M.; Abedzadeh, N.; Walia, J.; Patchett, S.; Saini, S. S. Color Matrix Refractive Index Sensors Using Coupled Vertical Silicon Nanowire Arrays. *Nano Lett.* **2012**, *12*, 4228–4234.
25. Wells, S. M.; Merkulov, I. A.; Kravchenko, I. I.; Lavrik, N. V.; Sepaniak, M. J. Silicon Nanopillars for Field-Enhanced Surface Spectroscopy. *ACS Nano* **2012**, *6*, 2948–2959.
26. Dayeh, S. A.; Picraux, S. T. Direct Observation of Nanoscale Size Effects in Ge Semiconductor Nanowire Growth. *Nano Lett.* **2010**, *10*, 4032–4039.
27. Bäuerle, D.; Irsigler, P.; Leyendecker, G.; Noll, H.; Wagner, D. Ar^+ Laser-Induced Chemical Vapor-Deposition of Si from SiH_4. *Appl. Phys. Lett.* **1982**, *40*, 819–821.
28. Bäuerle, D. *Laser Processing and Chemistry*, 3rd ed.; Springer: Berlin, 2000.
29. Kotecki, D. E.; Herman, I. P. A Real-Time Monte-Carlo Simulation of Thin-Film Nucleation in Localized-Laser Chemical Vapor-Deposition. *J. Appl. Phys.* **1988**, *64*, 4920–4942.
30. Hwang, D. J.; Ryu, S. G.; Grigoropoulos, C. P. Multi-Parametric Growth of Silicon Nanowires in a Single Platform by Laser-Induced Localized Heat Sources. *Nanotechnology* **2011**, *22*, 803106.
31. Hwang, D. J.; Ryu, S. G.; Kim, E.; Grigoropoulos, C. P.; Carraro, C. On Demand-Direct Synthesis of Si and Ge Nanowires on a Single Platform by Focused Laser Illumination. *Appl. Phys. Lett.* **2011**, *99*, 123109.
32. Jagannathan, H.; Deal, M.; Nishi, Y.; Woodruff, J.; Chidsey, C.; McIntyre, P. C. Nature of Germanium Nanowire Heteroepitaxy on Silicon Substrates. *J. Appl. Phys.* **2006**, *100*, 024318.

33. Adhikari, H.; Marshall, A. F.; Chidsey, C. E. D.; McIntyre, P. C. Germanium Nanowire Epitaxy: Shape and Orientation Control. *Nano Lett.* **2006**, *6*, 318–323.
34. Greytak, A. B.; Lauhon, L. J.; Gudiksen, M. S.; Lieber, C. M. Growth and Transport Properties of Complementary Germanium Nanowire Field-Effect Transistors. *Appl. Phys. Lett.* **2004**, *84*, 4176–4178.
35. Pauleau, Y.; Tonneau, D. Kinetics and Reaction Mechanisms of Laser-Assisted Chemical Vapor Deposition of Polycrystalline Silicon Dots from Silane. *J. Appl. Phys.* **2002**, *91*, 1553–1559.
36. Krylyuk, S.; Davydov, A. V.; Levin, I. Tapering Control of Si Nanowires Grown from $SiCl_4$ at Reduced Pressure. *ACS Nano* **2011**, *5*, 656–664.
37. Hannon, J. B.; Kodambaka, S.; Ross, F. M.; Tromp, R. M. The Influence of the Surface Migration of Gold on the Growth of Silicon Nanowires. *Nature* **2006**, *440*, 69–71.
38. Hertog, M. I.; Rouviere, J. L.; Dhalluin, F.; Desre, P. J.; Gentile, P.; Ferret, P.; Oehler, F.; Baron, T. Control of Gold Surface Diffusion on Si Nanowires. *Nano Lett.* **2008**, *8*, 1544–1550.
39. Ross, F. M.; Tersoff, J.; Reuter, M. C. Sawtooth Faceting in Silicon Nanowires. *Phys. Rev. Lett.* **2005**, *95*, 146104.
40. Hild, R.; Seifert, C.; Kammler, M.; Heringdorf, F.; Horn-von-Hoegen, M.; Zhachuk, R. A.; Olshanetsky, B. Z. Kinetics of Au Induced Faceting of Vicinal Si(111). *Surf. Sci.* **2002**, *512*, 117–127.
41. Seehofer, L.; Huhs, S.; Falkenberg, G.; Johnson, R. L. Gold-Induced Faceting of Si(111). *Surf. Sci.* **1995**, *329*, 157–166.
42. Oehler, F.; Gentile, P.; Baron, T.; Ferret, P.; Den Hertog, M.; Rouviere, J. The Importance of the Radial Growth in the Faceting of Silicon Nanowires. *Nano Lett.* **2010**, *10*, 2335–2341.
43. Boukhicha, R.; Gardes, C.; Vincent, L.; Renard, C.; Yam, V.; Fossard, F.; Patriarche, G.; Jabeen, F.; Bouchier, D. Gold Anchoring on Si Sawtooth Faceted Nanowires. *EPL* **2011**, *95*, 18004.
44. Hirayama, H.; Hiroi, M.; Ide, T. {311} Facets of Selectively Grown Epitaxial Si Layers on Sio2-Patterned Si(100) Surfaces. *Phys. Rev. B* **1993**, *48*, 17331–17337.
45. David, T.; Buttard, D.; Schulli, T.; Dallhuin, F.; Gentile, P. Structural Investigation of Silicon Nanowires Using Gixd and Gisaxs: Evidence of Complex Saw-Tooth Faceting. *Surf. Sci.* **2008**, *602*, 2675–2680.
46. Frolov, T.; Mishin, Y. Temperature Dependence of the Surface Free Energy and Surface Stress: An Atomistic Calculation for Cu(110). *Phys. Rev. B* **2009**, *79*, 174110.
47. Wiethoff, C.; Ross, F. M.; Copel, M.; Hoegen, M. H. V.; Heringdorf, F. Au Stabilization and Coverage of Sawtooth Facets on Si Nanowires Grown by Vapor-Liquid-Solid Epitaxy. *Nano Lett.* **2008**, *8*, 3065–3068.
48. Eaglesham, D. J.; White, A. E.; Feldman, L. C.; Moriya, N.; Jacobson, D. C. Equilibrium Shape of Si. *Phys. Rev. Lett.* **1993**, *70*, 1643–1646.
49. Tomioka, K.; Motohisa, J.; Hara, S.; Fukui, T. Control of Inas Nanowire Growth Directions on Si. *Nano Lett.* **2008**, *8*, 3475–3480.
50. Ng, K. W.; Ko, W. S.; Tran, T. D.; Chen, R.; Nazarenko, M. V.; Lu, F.; Dubrovskii, V. G.; Kamp, M.; Forchel, A.; Chang-Hasnain, C. J. Unconventional Growth Mechanism for Monolithic Integration of III-V on Silicon. *ACS Nano* **2013**, *7*, 100–107.
51. Glas, F. Critical Dimensions for the Plastic Relaxation of Strained Axial Heterostructures in Free-Standing Nanowires. *Phys. Rev. B* **2006**, *74*, 121302.
52. Cirlin, G. E.; Dubrovskii, V. G.; Soshnikov, I. P.; Sibirev, N. V.; Samsonenko, Y. B.; Bouravleuv, A. D.; Harmand, J. C.; Glas, F. Critical Diameters and Temperature Domains for Mbe Growth of III-V Nanowires on Lattice Mismatched Substrates. *Phys. Status Solidi RRL* **2009**, *3*, 112–114.
53. Seo, K.; Wober, M.; Steinvurzel, P.; Schonbrun, E.; Dan, Y.; Ellenbogen, T.; Crozier, K. B. Multicolored Vertical Silicon Nanowires. *Nano Lett.* **2011**, *11*, 1851–1856.
54. Sanchez-Iglesias, A.; Pastoriza-Santos, I.; Perez-Juste, J.; Rodriguez-Gonzalez, B.; Garcia de Abajo, F. J.; Liz-Marzan, L. M. Synthesis and Optical Properties of Gold Nanodecahedra with Size Control. *Adv. Mater.* **2006**, *18*, 2529–2534.
55. Bruchez, M.; Moronne, M.; Gin, P.; Weiss, S.; Alivisatos, A. P. Semiconductor Nanocrystals as Fluorescent Biological Labels. *Science* **1998**, *281*, 2013–2016.